

Efficient production of sodium Bose-Einstein condensates in a hybrid trap

Y. Geng , ^{a)} S. Mukherjee , ^{a)} S. Banik  M. Gutierrez Galan, ^{1,3} M. Anderson , ¹
H. Sosa-Martinez , ^{1,4} S. Eckel  I. B. Spielman , ^{1,5, b)} and G. K. Campbell , ^{1,5, c)}

¹⁾Joint Quantum Institute, University of Maryland and National Institute of Standards and Technology, College Park, Maryland, 20742, USA

²⁾Lightmatter Inc., California 94040, USA

³⁾IonQ, College Park, Maryland, 20742, USA

⁴⁾Capital One, McLean, Virginia 22102, USA

⁵⁾National Institute of Standards and Technology, Gaithersburg, Maryland, 20899, USA

(Dated: 13 June 2025)

We describe an apparatus that efficiently produces ^{23}Na Bose-Einstein condensates (BECs) in a hybrid trap that combines a quadrupole magnetic field with a far-detuned optical dipole trap. Using a Bayesian optimization framework, we systematically optimize all BEC production parameters in modest sized batches of highly correlated parameters. Furthermore, we introduce a Lagrange multiplier-based technique to optimize the duration of different evaporation stages constrained to have a fixed total duration; this enables the progressive creation of increasingly rapid experimental sequences that still generate high quality BECs. Taken together, our techniques constitute a general approach for refining and accelerating sequence-based experimental protocols.

I. INTRODUCTION

Since their first experimental realization in 1995^{1,2}, atomic Bose-Einstein condensates (BECs) have become a workhorse system for studying a diverse range quantum many-body phenomena^{3–5} including: open quantum systems⁶, quantum gases in low dimensions^{7–11}, and cosmological as well as gravitational physics^{12–20}. This breadth of applications has been accompanied by generations of increasingly sophisticated apparatuses, each incorporating new techniques for cooling, control, and measurement. Quantum gas experiments nearly universally operate in a cyclic manner, where each repetition creates a quantum gas that is then manipulated, measured, and in the process destroyed. Cutting-edge experiments require very large data sets—making short cycle times highly desirable—and demand a high degree of stability with minimal drift in experimental conditions.

The overall cycle time is often dominated by the preparation process, which can take tens of seconds. Once the quantum gas is created, the subsequent physics experiment can take anywhere from a few microseconds to many tens of seconds. As a result, the preparation time is often the bottleneck for employing quantum degenerate gases in both applied and fundamental applications. An increased data rate enables more effective exploratory studies, yields larger datasets for reduced statistical noise, lowers Dick sampling noise²¹ for precision measurements, and reduces sensitivity to systematic drifts. Thus, quantum gas production techniques that reduce production time and increase stability are essential

for further applications of this platform. In this paper, we begin by briefly describing our experimental apparatus for generating ^{23}Na BECs; we then detail several strategies for optimally creating BECs while simultaneously minimizing the production time.

Quantum degenerate gases are almost always produced in a two-stage process consisting of laser cooling followed by evaporative cooling. All such experiments include a magneto-optical trap (MOT) as part of the laser cooling process to prepare an initial sample of cold atoms. In some cases, such as ours, this MOT collects atoms from a cold atomic beam (e.g., from a Zeeman slower, a 2D-MOT, or a buffer gas source), while in others atoms are captured directly from the low velocity tail of a dilute room-temperature vapor. In our experiment, the MOT temperature is fairly high (approximately $290\ \mu\text{K}$), so we include a sub-Doppler cooling stage that reduces the temperature to about $\approx 40\ \mu\text{K}$ before transferring the atoms to a conservative potential (here, a magnetic trap) for the evaporative cooling stage. Sub-Doppler cooling in ^{23}Na leaves the sample well above the typical $\approx 5\ \mu\text{K}$ BEC transition temperature, thereby requiring efficient evaporative cooling. Evaporative cooling selectively removes the most energetic atoms while elastic collisions rethermalize the remainder at a reduced temperature. Because collision rates in these dilute gases are relatively low, evaporative cooling typically accounts for the majority of the total production time. A primary focus of this paper is therefore to optimize evaporation performance subject with a constrained total evaporation time.

Given the clear delineation between initial laser cooling and the subsequent evaporation, we quantify the evaporation stage's performance by introducing the production efficiency $N_{\text{BEC}}/N_{\text{MOT}}$. This ratio reflects how effectively a cloud of N_{MOT} laser-cooled atoms is converted into a fully condensed BEC of N_{BEC} atoms. Figure 1 plots production efficiency as a function of the evapo-

^{a)}These authors contributed equally to this work.

^{b)}Electronic mail: ian.spielman@nist.gov

^{c)}Electronic mail: gretchen.campbell@nist.gov

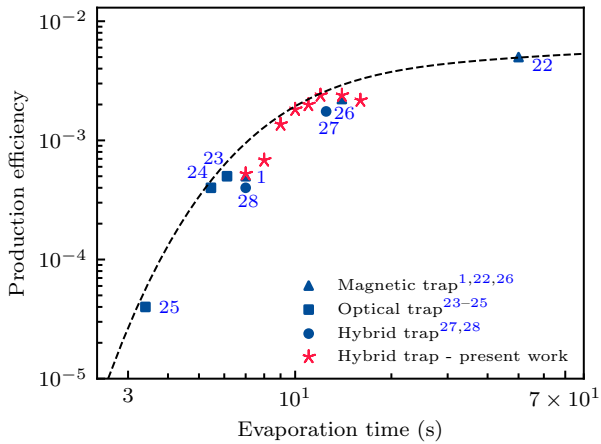


FIG. 1. Comparison of different sodium BEC machines' production efficiency and evaporation time. Different symbols identify the underlying trapping employed used during evaporation: magnetic traps (triangles), all-optical traps (squares), and hybrid magnetic-optical traps (circles, with our system in red). In addition the dashed curve serves as a guide to the eye, indicating the nominal performance limit of existing systems in the efficiency- t_{evap} plane.

tion time t_{evap} (rather than total cycle time) for various ^{23}Na BEC apparatuses, thereby isolating the effect of evaporation from any complexities in MOT loading. Because the MOT loading time strongly depends on variables such as the atomic source, laser power, and beam geometry, we treat it as largely independent of evaporation optimization. Nonetheless, in the outlook we briefly note how coupling these two stages could provide further performance gains.

Harmonically confining magnetic traps generated by large, out of vacuum, coils feature very large trap volumes but with correspondingly gentle confinement^{22,29}. As a result, they yield the largest N_{BEC} , but also require large t_{evap} due to their low atom densities, and corresponding low collision rates. These low densities decrease 2- and 3-body loss processes, contributing to their high efficiencies.

In contrast, purely optical traps^{23–25,30} achieve very strong confinement; while this enables rapid evaporation, the resulting BECs are small due to limited trap volume, and enhanced three-body losses. Similarly in ^{87}Rb , magnetic chip traps^{31,32} offer strong confinement in a compact geometry, and generate small BECs with cycle times as short 1 s.

Hybrid traps, initially developed for ^{87}Rb , merge the strengths of magnetic and optical dipole traps (ODTs): first capturing atoms in a large-volume magnetic trap, and subsequently transferring them to a tightly confining optical trap^{28,33–35}. In Fig. 1, they occupy an intermediate performance regime, achieving large N_{BEC} together with modest t_{evap} . Notably, Ref. 1 employed an optically plugged quadrupole magnetic trap that achieved similar

performance, but was rapidly abandoned owing to alignment instability. In these cases the same higher density that reduces the evaporation time also accelerates 2- and 3- body loss processes.

For all of these approaches, BECs are produced through a sequence of experimental stages each with a set duration, during each of which parameters—quantifying the power and frequency of optical, microwave and RF electromagnetic fields, the strength and direction of (near) DC magnetic fields, to name just a few—follow preselected ramps. Efficient BEC production therefore requires not only a carefully chosen hardware configuration, but also careful optimization of the stage durations and parameter values. After manually establishing a preliminary parameter set, we employ a Bayesian optimization framework M-LOOP introduced in Ref. 36 that is known to be performant for cold atom experiments^{36–39}. In isolation Bayesian optimization suffers from the “curse of dimensionality,” leading to slow convergence (or none at all) when more than a handful of parameters are involved. We address this by measuring the parameters’ covariance matrix, grouping strongly correlated parameters, and then employing Bayesian optimization to these groups sequentially.

This approach is effective in generating the globally optimal parameter set; however, it is unable to support algebraic constraints, such as optimizing the duration of each experimental stage subject to the constraint of fixed overall sequence duration. We therefore developed a Lagrange multiplier scheme to enforce such constraints, enabling us to optimize the range of fixed-duration evaporation sequences whose performance is shown in Fig. 1. Combining these approaches, we produced large BECs of $4.2(1) \times 10^6$ atoms, starting with $1.8(1) \times 10^9$ atoms in the MOT, after 12 s of evaporation, and still yielded $9.2(1) \times 10^5$ atom BECs using just 7 seconds of evaporation.

The remainder of the manuscript is organized as follows. In Sec. II, we provide an overview of our experimental design at the hardware level. Then in Sec. III, we outline our BEC production sequence. Next, Sec. IV details our optimization protocol. Finally, we conclude in Sec. V.

II. SYSTEM DESCRIPTION

Here we provide a high-level description of our apparatus including descriptions of the mechanical and optical setups. Further details can be found in Ph.D. thesis of S. Banik⁴⁰ and M. Gutierrez Galan⁴¹.

A. Vacuum System

The vacuum system (Fig. 2) comprises a “high” pressure 2D MOT source, connected via a low conductance link to a low-pressure UHV science chamber (giving a

vacuum-limited lifetime of magnetically trapped atoms ≈ 25 s).

2D MOT chamber – Our 2D MOT (Fig. 3), inspired by Ref. 42, is built around a ten-way ConFlat cross with four 2.75" and four 1.33" flanges in the cross's plane, plus individual 2.75" and 1.33" flanges on the axis normal to that plane (1" = 2.54 cm). The 2.75" out-of-plane flange connects to the pumping section, and the 1.33" flange connects to science chamber. Finally, a gate valve and a 3 mm-diameter differential pumping tube separate the atomic source region from the science chamber. A resistively-heated sodium oven is mounted on the bottom in-plane 1.33" flange.

The 2D MOT's quadrupole field is produced by four stacks of nine 25 mm \times 10 mm \times 3 mm neodymium bar magnets [Eclipse N750-RB⁴³, with magnetization $(8.8 \pm 0.1) \times 10^5$ A m⁻¹] mounted on the cross^{42,44}. The stacks are divided into front and back sets spaced by 70 mm, and each set contains two stacks that are vertically separated by 98 mm. These result in a 2D quadrupole field with a 0.42 T/m gradient; this gradient changes by only ≈ 10 % over the longitudinal extent of the 2D MOT.

Science chamber – The science chamber (Kimball Physics MCF800-SphSq-G2F1E3C4A16) is an 8" stainless-steel vessel with recessed windows on the top and bottom. Four 4.5" and four 2.75" flanges reside on the horizontal plane and eight pairs of 1.33" flanges are placed 21° above and below the horizontal plane. The recessed windows' inner surfaces are setback by 20 mm from the chamber's center.

Magnetic field gradients for the 3D MOT and magnetic trap are generated by a pair of coils in an anti-Helmholtz configuration. Each coil is wound from Kapton insulated 3/16" (0.48 cm) hollow square copper tube and is mounted just outside a recessed window. At the peak current of 200 A, these coils provide a 0.11 mT cm⁻¹ gradient along e_z and are water-cooled with a flow rate of 0.6 L min⁻¹, supplied by a booster pump operating at 1.25 MPa (180 psi). Finally, three additional pairs of coils in a Helmholtz configuration provide bias magnetic fields along each Cartesian axis.

The 2D MOT chamber is actively pumped by an hybrid ion-getter pump (SAES D-100), and the science chamber is pumped by a combination of an ion pump (Gamma Vacuum 45S) and an hybrid ion-getter pump(SAES D-500). A titanium sublimation pump is attached to the science chamber but was only activated during the initial pump-down phase.

B. Optical sources

All of the laser light used for laser cooling, imaging, and repumping is derived from two lasers resonant with distinct transitions within ²³Na's 589 nm D₂ line. The first, a Toptica DL-RFA-SHG pro (1.1 W output power), addresses the $|F=2\rangle \rightarrow |F'=3\rangle$ cooling transition. The second, a Toptica TA-SHG pro (0.9 W output power),

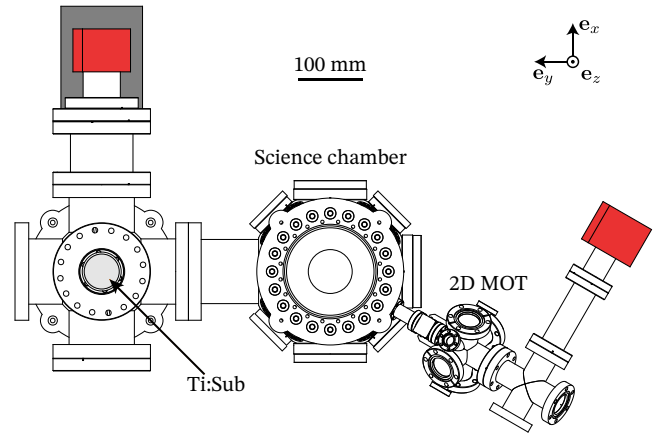


FIG. 2. Top view of vacuum system. Red/gray colored regions denote vacuum pumps with a standard ionization pump in dark gray, combination ionization/getter pumps in red, and a Ti:Sub pump in light gray.

MOT loading		
Beam	Frequency	Intensity
2D MOT cooling	$f_{2 \rightarrow 3} - 1.2\Gamma$	$1.9I_{\text{sat}}$
2D MOT repump	$f_{1 \rightarrow 2} - 1.5\Gamma$	$30.5I_{\text{sat}}$
Zeeman slower	$f_{2 \rightarrow 3} - 18.6\Gamma$	$23.1I_{\text{sat}}$
Push beam	$f_{2 \rightarrow 3} + 0.3\Gamma$	$0.05I_{\text{sat}}$
3D MOT cooling	$f_{2 \rightarrow 3} - 1.4\Gamma$	$1.7I_{\text{sat}}$
3D MOT repump	$f_{1 \rightarrow 2} - 1.1\Gamma$	$1.9I_{\text{sat}}$
sub-Doppler cooling		
Beam	Frequency	Intensity
3D MOT cooling	$f_{2 \rightarrow 3} - 3.4\Gamma$	$0.3I_{\text{sat}}$
Bright repump	$f_{1 \rightarrow 2} - 1.1\Gamma$	$0.1I_{\text{sat}}$
Optical pumping		
Beam	Frequency	Intensity
3D MOT cooling	$f_{2 \rightarrow 3} - 0.9\Gamma$	$0.3I_{\text{sat}}$
Optical pumping	$f_{1 \rightarrow 1} + 0.26\Gamma$	$0.007I_{\text{sat}}$

TABLE I. Set of laser parameters during each laser cooling stage. Frequencies are reported with respect to that of the desired transition (i.e., $f_{2 \rightarrow 3}$ denotes the frequency of the $|F=2\rangle \rightarrow |F'=3\rangle$ transition). Intensities are reported with respect to the saturation intensity of the $|F=2\rangle \rightarrow |F'=3\rangle$ transition.

couples to the $|F=1\rangle \rightarrow |F'=2\rangle$ repumping transition. The cooling laser is locked to a Doppler-free saturated absorption feature, while the repump laser is beat note-locked to the cooling laser with a 1.8 GHz frequency shift. All laser light is delivered to the vacuum system via single-mode optical fiber. The nominal laser parameters are summarized in Table I.

2D MOT lasers – Our 2D MOT utilizes in-plane “cooling” beams, a repump beam, a Zeeman slower beam and a transverse push beam. The two retro-reflected cooling beams (≈ 6 mm waist) enter and exit the 2D MOT chamber via the four in-plane 2.75" viewports. The repump and the Zeeman slower beams are overlapped, enter the chamber through the top 1.33" viewport, and pass through the 2D MOT before entering the Na oven. Lastly, the push beam has a 1 mm waist and enters the chamber by the longitudinal axis 2.75" viewport (i.e. oriented along the longitudinal axis of the 2D MOT directed into the science chamber).

MOT lasers – A 2-in, 6-out fiber beam splitter (Evanescent Optics) then distributes light injected into a single fiber to the six outputs that source the 3D MOT / sub-Doppler cooling beams with waist ≈ 12 mm). Repumping during dark SPOT MOT operation is provided by a single beam (with waist ≈ 8 mm) with a 9 mm diameter dark spot imaged onto the MOT center. In addition a single “bright” (i.e., no dark spot) repump illuminates the atoms during sub-Doppler cooling.

Optical pumping laser – The optical pumping beam is derived from the same laser system as the MOT repump light, frequency-shifted by an acousto-optical modulator to address the $|F = 1\rangle \rightarrow |F' = 2\rangle$ transition. It is sent along the quantization axis set by a uniform bias magnetic field ≈ 0.1 mT with a waist of approximately 4 mm and power 40 μ W.

ODT laser – The 1064 nm ODT beam is produced by Ytterbium fiber laser (IPG YLR20-1064-LP-SF). After pre- and post-conditioning along with coupling through a polarization-maintaining photonic crystal fiber (NKT LMA-PM-10) with ≈ 70 % efficiency, 6.3 W of power is delivered to the vacuum system. The beam then enters through the 4.5" viewport on the y -axis is focused to a $1/e^2$ waist of 22 μ m, forming an ODT with a maximum depth of 200 μ K.

C. UV desorption source

We employ light-induced atomic desorption (LIAD) to inhibit Na buildup on the top 2.75" 2D MOT windows^{45,46}. This light is sourced from a pair of LED lamps (Thorlabs M365LP1) and is merged into the MOT beams via dichroic beam splitters yielding 30 mW at each viewport.

III. SYSTEM OPERATION

In brief, our BEC production begins with a 2D-MOT that generates a cold atomic beam from a hot effusive ^{23}Na source. The cold beam then travels into the science chamber where ^{23}Na atoms are captured into a dark spontaneous-force optical trap (SPOT⁴⁷, although duplicative we will conform to the standard language of “dark SPOT MOT”). Afterward they are sub-Doppler

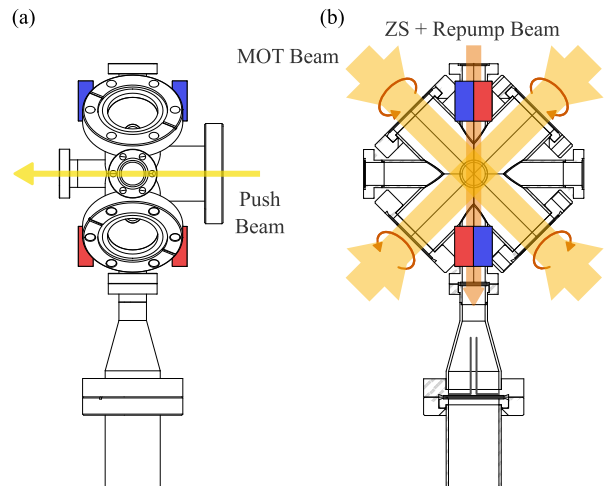


FIG. 3. 2D MOT. (a) Front view. Laser beams are colored in yellow. The north and south poles of magnets are colored in red and blue, respectively. (b) Side-section view. The polarization is marked on two MOT beams. Zeeman slower beam is polarized perpendicular direction of the drawing.

cooled⁴⁸, and finally optically pumped into the magnetically trappable low field seeking state $|F = 1, m_F = -1\rangle$.

We abruptly turn on a quadrupole magnetic trap, where the atoms undergo rf-evaporation. Once the cloud becomes sufficiently cold and dense, it is transferred into a horizontally aligned single-beam ODT³³. Forced evaporation by lowering the ODT power brings the sample to quantum degeneracy.

A. 2D MOT

The Na oven, operating at ≈ 240 °C, directs an up-going atomic beam into the 2D MOT. Owing to Na’s low vapor pressure this can rapidly coat the top 1.33" viewport, which we prevent by continuously heating the top viewport to 130 °C. Over longer timescales Na also accumulates on the in-plane 2.75" 2D MOT cooling viewports. We prevent this accumulation via nightly exposure to the UV LIAD light.

The decreasing fringe field from the 2D MOT permanent magnets resembles the field profile of a traditional Zeeman slower as it rises from 0 mT to a maximum of 20 mT over a distance of about 50 mm. Motivated by this observation⁴², our cooling process begins by Zeeman-slowing the Na atomic beam using a red-detuned down-going slower beam. The slowed atomic beam is then captured and cooled into the 2D MOT before being directed towards the 3D MOT by the blue-detuned push beam. This configuration relies on a single repump beam—co-propagating with the slower beam and detuned by 9 MHz from the $|F = 1\rangle \rightarrow |F' = 2\rangle$ transition—for both the slowing and 2D cooling stages. We operate this beam at fairly high power to provide effective repumping for both, given the poor transmission of the viewport.

B. Dark SPOT MOT

After entering the science chamber, the cold atomic beam from the 2D MOT is captured by the dark SPOT MOT. During this stage, the quadrupole magnetic field has a z -axis gradient of 0.6 mT/cm . The three pairs of counterpropagating MOT beams are red-detuned from the $|F = 2\rangle \rightarrow |F' = 3\rangle$ cycling transition and the two intersecting dark-SPOT repump beams are red-detuned from the $|F = 1\rangle \rightarrow |F' = 2\rangle$ transition. In the dark volume at the interaction of these beams atoms accumulate in the ground state $|F = 1\rangle$ manifold reducing the radiation pressure and increasing the maximum atomic density⁴⁷.

All together we observe an initial atom loading rate of $0.8 \times 10^9 \text{ s}^{-1}$ and the MOT number saturates at 2×10^9 after about 10 s. In practice we load the MOT for 7 s yielding 1.8×10^9 atoms at $\approx 290 \mu\text{K}$.

C. Sub-Doppler cooling

After MOT loading, we perform sub-Doppler cooling by: removing the magnetic field gradient; further red-detuning the MOT beams and reducing their intensity; and use the bright repump beam for uniform repumping. During this stage, stray magnetic fields are canceled using the bias coils. The atoms cool to $\approx 40 \mu\text{K}$ in just 2 ms and are fully depumped into the $|F = 1\rangle$ manifold.

D. Hybrid trap loading

Prior to magnetic trapping, the sub-Doppler cooled cloud nominally uniformly populates all three magnetic sublevels of the $|F = 1\rangle$ manifold; of these states, only the $|F = 1, m_F = -1\rangle$ is a magnetically trappable weak-field seeking state. We therefore optically pump into $|F = 1, m_F = -1\rangle$ in 1.2 ms using a low intensity (0.02 mW/cm^2) circularly polarized optical pumping beam driving the $|F = 1\rangle \rightarrow |F' = 1\rangle$, aligned to an $\approx 0.1 \text{ mT}$ bias field along with depumping from the MOT beams²².

After optical pumping, we suddenly energize the quadrupole trap to a gradient of 7.3 mT/cm , capturing 60 % of the atoms. The trapped ensemble is then compressed by increasing the gradient to 19 mT/cm in 240 ms, adiabatically increasing the temperature to $\approx 230 \mu\text{K}$, at a nominally fixed phase space density of 10^{-5} (Fig. 4d). The ODT is then turned on to its peak power of $\approx 6 \text{ W}$; at this time it contributes only a small perturbation (trap depth $\approx 200 \mu\text{K}$) to the magnetic trap.

E. Evaporative cooling

After laser cooling, we use evaporative cooling to bring the atoms to quantum degeneracy. Figure 4 shows our

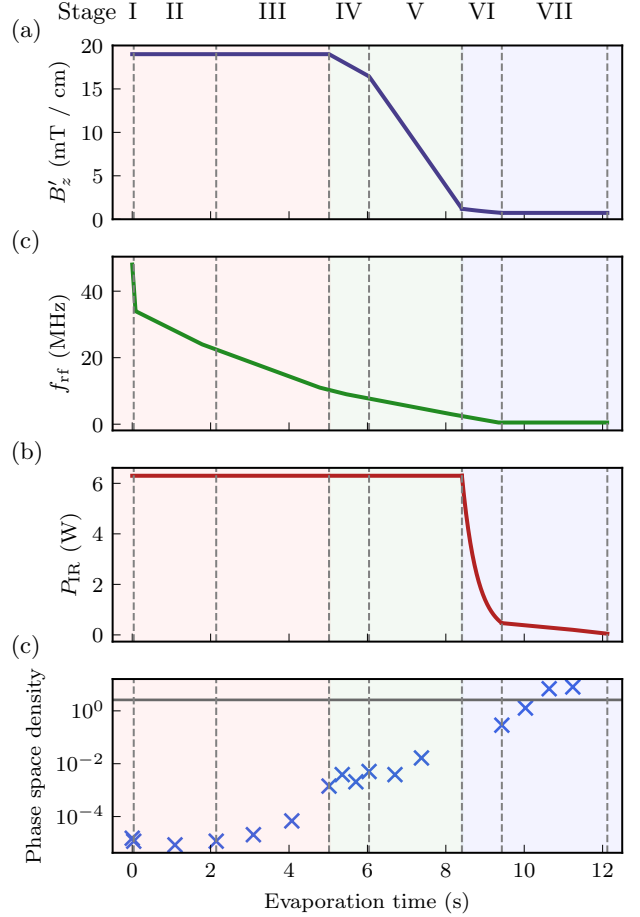


FIG. 4. The evaporation sequence. z -axis quadrupole field gradient B_z' , rf frequency f_{rf} , and ODT beam power P_{IR} as a function of time into the evaporation sequence are shown in (a), (b), and (c). The sequence is divided into ramps, whose boundaries are indicated by the gray dash lines. The red, green, and blue shaded regions represent the rf evaporation stage, the decompression/transfer stage, and the hybrid trap evaporation stage, respectively. (d) shows the phase space density calculated from the experimental data. The gray solid line marks the BEC transition's critical phase space density of ≈ 2.6 .

optimized evaporation sequence (see Sect. IV) that leads to our largest BECs.

First, we perform rf-evaporation in a purely magnetic quadrupole trap, which uses an oscillating magnetic field. If the atoms' Zeeman shift equals the frequency of the rf magnetic field, their internal state is changed from $|F = 1, m_F = -1\rangle$ to $|F = 1, m_F = 0, +1\rangle$ and they are ejected from the trap. At the beginning of the re-evaporation stage, our initial frequency of 48 MHz is quickly swept from 48 MHz to 34 MHz in 0.05 s, then slowly reduced to 11 MHz in 4.8 s, resulting in a cloud of approximately 50×10^6 atoms with temperature $\approx 80 \mu\text{K}$.

Near the end of the rf evaporation process we reduce the magnetic confinement (green region in Fig. 4), allow-

ing the ODT (placed just below the quadrupole center) to provide vertical support against gravity. Because the ODT contributes a dimple-like potential to the horizontal magnetic confinement, even adiabatic transfer leads to the increase in phase-space density⁴⁹ seen in Fig. 4. During the hybrid trap evaporation stage (blue region in Fig. 4), the ODT depth is ramped down from $\approx 200 \mu\text{K}$ to $17 \mu\text{K}$ following an exponential ramp and a linear ramp with combined duration of 4.2 s. About half-way through this stage, the phase-space density of the atoms crosses the critical phase density of 2.6, at which point a BEC first forms⁵⁰. The sequence concludes with an almost-pure BEC with $4.2(1) \times 10^6$ atoms confined in a the hybrid trap with frequencies: $\omega_\rho = 2\pi \times 320 \text{ Hz}$ (radial confinement from ODT) and $\omega_x = 2\pi \times 22 \text{ Hz}$ (longitudinal confinement from combined magnetic and optical potentials).

IV. OPTIMIZATION

As seen in Sec. III, each separate experimental stage requires a range of control and timing parameters, that are often correlated between stages. All of these inter-dependent parameters must be optimized for peak performance. Optimization can be abstracted as minimizing one or more “cost functions” that characterize the system’s performance for a particular a set of control parameters. Brute force optimization quickly becomes intractable in the face of a large number of strongly correlated control parameters, an associated convoluted cost function landscape, measurement noise, and of course hardware-level technical limitations. It is virtually impossible to construct a top-to-bottom first-principle theoretical description of a cold-atom apparatus; as such this optimization is largely empirical but guided by theory and modeling.

Traditional optimization methods operate by sampling from and navigating the cost landscape in an attempt to locate the (global) minimum. Many contemporary approaches now frame this as a machine learning (ML) task, with the objective transformed into “learning” a high quality model of the underlying physical reality, from which extrema can be accurately identified. Gaussian processes (GP), a type of Bayesian optimization, is one such approach; while this has already yielded promising results in cold-atom experiments^{36,37,39}, many challenges remain. For instance, these optimization methods suffer from the curse of dimensionality and scale poorly with increasing parameter-count in two ways: (1) Even in principle, the required number of samples rapidly increases (thereby increasing the requisite computational resources for Bayesian inference); and (2) in conjunction with experimental noise, large-parameter count GP models can often fail to converge. Furthermore, like most ML approaches, the performance of these methods depends strongly on the choice of hyperparameters⁵¹, and the mechanism (if any) of in-loop hyperparameter tuning

as the cost function landscape is explored.

We developed a multi-stage optimization procedure to circumvent the curse of dimensionality. This procedure begins by manual scanning each parameter to identify an initial value and bounds for the following optimization. Next, these parameters are grouped into (potentially) intuitively related sets—*e.g.*, “laser cooling” or “ODT evaporation”—of about 10 parameters and optimized with GP. We then use a stochastic sampling technique to compute the parameter correlation matrix, allowing us to quantitatively collect parameters into sets with strong intra-set correlations and weak inter-set correlations, which are then separately optimized.

Introducing user-defined algebraic constraints to this optimization task is a further challenge. This is commonly implemented by adding a penalty term to the cost function^{37,52}. While effective, this technique requires careful tuning of the relative strength of the penalty with respect to the remainder of the cost function: an excessive penalty can cause the optimizer to diverge, while too little will be ignored. Instead, we constrained the optimization task by including a Lagrange multiplier in the cost function. When constraining the total evaporation time, such a method enables the production of high-quality BECs with progressively shorter experimental durations.

In the remainder of this section, we describe separate strategies to effectively optimize large parameter sets (Sec. IV A) and incorporate algebraic constraints (Sec. IV C).

A. Parameter grouping

Our focus is on ML optimization tasks where experimental data acquisition rate is low (limiting the number of samples) and computational requirements scale poorly with the dimension of the parameter space. In general, this situation is hopeless and giving up is likely the most rational response. Experimentalists are not known for such sensible behavior, and besides, in laboratory settings even a highly non-trivial cost function landscape may contain some hidden structure. In our case, this structure is encoded in correlations between control parameters: parameters that are highly correlated in the neighborhood of one critical point (local minima, maxima, or saddle point) are likely to be correlated near another. This converts a hopeless situation into a hopeful three-step process of: identifying at least one critical point, obtaining the parameter’s correlation matrix at that location, and optimizing parameters in sets with strong correlations.

During the setup stage of any real experiment, every control parameter is likely to have been studied at least once; for each parameter, this provides working information regarding its nominal optimal operating point, and overall range of utility. Taken together, this set of nominal optimal operating points identifies a critical point in

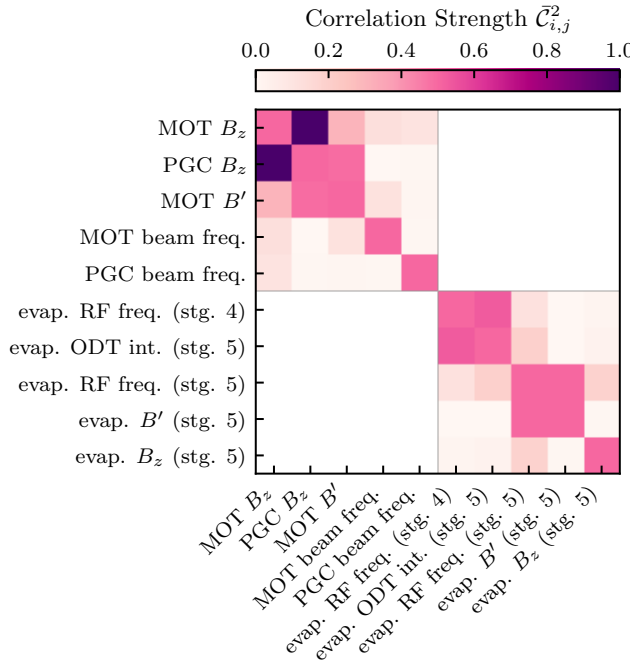


FIG. 5. Control parameter correlations. These parameters include those used for laser cooling, and transfer into the hybrid trap. The strength of correlations is represented by the color of the off-diagonal terms. Each row and column is normalized by the value of the diagonal term (see text).

parameter space with zero gradient of the fitness function along all directions, therefore suitable to explore the correlation matrix. In practice, we employed several rounds of human-guided manual tuning and GP optimization to identify the initial operating point, denoted by the vector $x_i^{(0)}$ in parameter space.

We then randomly sample the cost function at points $\mathbf{x}^{(n)}$ in the neighborhood of the initial operating point, i.e, small $\Delta x_i^{(n)} \equiv x_i - x_i^{(0)}$, and fit a second-order polynomial

$$C(\Delta x_i) \approx \mathcal{A} + \sum_i \mathcal{B}_i \Delta x_i + \sum_{i,j} \Delta x_i \mathcal{C}_{i,j} \Delta x_j \quad (1)$$

to the resulting data. Here \mathcal{A} measures the nominal value of the cost function, \mathcal{B}_i is the local gradient [ideally zero, at $x_i^{(0)}$], and $\mathcal{C}_{i,j}$ is the desired covariance matrix. The diagonal elements of $\mathcal{C}_{i,j}$ quantify the individual parameter sensitivities, and the off-diagonal elements describe cross-correlations. Because the parameter sensitivities are completely arbitrary (given by whatever units happen to be used in the experimental control system), we quantify parameter correlations in terms of squared normalized correlation matrix $\bar{\mathcal{C}}_{i,j}^2 \equiv \mathcal{C}_{i,j}^2 / (\mathcal{C}_{i,i} \mathcal{C}_{j,j})$ whose diagonal elements have been scaled to unity.

Figure 5 illustrates $\bar{\mathcal{C}}_{i,j}^2$ for two sets of parameters taken from two very different parts of the experimental sequence: the first set includes parameters from the laser

cooling stages, while the other contains parameters from the hybrid trap transfer stage. As perhaps intuitively expected, only parameters within these sets are correlated. However, even within these sets, specific parameters exhibit differing degrees of correlation.

Laser cooling parameters—the bias and gradient magnetic fields during the MOT loading and sub-Doppler cooling stages are strongly correlated; this arises from the slow response time of the coils. By contrast, the laser detunings during the MOT loading and sub-Doppler cooling stages control very different processes and are weakly correlated.

Hybrid trap transfer parameters—The magnetic trap gradient and rf frequencies are highly correlated as their interplay controls the evaporation efficiency. Likewise, the rf frequency and the ODT intensity are strongly correlated because the rf frequency sets the temperature of the cloud which the ODT must then be deep enough to capture.

In the end, experimentally identified correlations such as these are used to partition the whole parameter set into strongly correlated subsets that are optimized together.

B. Bayesian optimization

We employ a GP based Bayesian optimizer which is particularly effective in settings where sampling the cost function is expensive, the number of sampled points is restricted, and experimental noise is present.

At every optimization, a GP optimizer encodes a probability distribution over the set of all potential cost functions $\{f(\mathbf{x})\}$, where the probability density of a specific cost function is given by a (functional) normal distribution. The task of the GP model is to identify a best choice of the distribution's \mathbf{x} -dependent mean $\mu^{(n)}(\mathbf{x})$ and width $\sigma^{(n)}(\mathbf{x})$ given information available at iteration n . In practice this problem is still intractable, so to reduce the search space GP models employ correlation length hyperparameters that describe the range in every direction of parameter space over which functions are likely to exhibit correlations. At each iteration, a GP model generally uses the most likely function $C_{\text{GP}}^{(n)}(\mathbf{x}) = \mu^{(n)}(\mathbf{x})$ as the estimated cost function.

Given a GP model at iteration n , a numerical optimization algorithm determines the next parameter vector $\mathbf{x}^{(n+1)}$ to be sampled. One common choice is the upper confidence bound criterion: $\mathbf{x}^{(n+1)} = \text{argmin} \{\mu(\mathbf{x}^{(n)}) + \alpha \sigma(\mathbf{x}^{(n)})\}$, where the hyperparameter α balances pursuing the minimum and exploring the unknown region of the model and is dynamically regulated during the optimization procedure. The potential optimal $\mathbf{x}^{(n+1)}$ is experimentally measured, yielding $C_m(\mathbf{x}^{(n+1)})$, the GP parameters are updated, and the process repeats with a new parameter vector. This iterative procedure continues until a termination criterion is met, such as a predefined number of iterations or convergence to an optimal

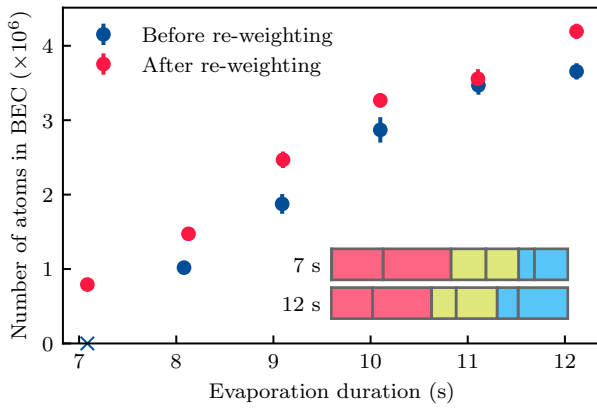


FIG. 6. Evaporation sequence performance. The blue/red dots mark the performance of the initial sequence before/after re-weighting. The blue cross at 7 s indicates that the sequence before re-weighting utterly failed in producing a BEC. The two bars in the inset show the percentage of time spent in each stage for the optimal 7 s and 12 s sequence. The red, green, and blue region marks the rf evaporation stage, the decompression/transfer stage, and the hybrid trap evaporation stage, respectively.

parameter set.

We employ the open-source package ‘Machine-Learning Online Optimization Package’ (M-LOOP)³⁶ to implement the GP optimization and interface it with our **labscript**-based⁵³ experiment control system. M-LOOP is seeded with an initial dataset obtained by experimentally sampling the cost at parameter vectors $\mathbf{x}^{(n)}$. The set of vectors might be selected: at random, with a different optimizer like differential evolution (our choice), or even with a previous GP model. The measured points help to update GP model’s hyperparameters. The GP optimizer allows us to efficiently explore the multiparameter space by prioritizing regions with higher uncertainty, unlike regular grid scans that uniformly sample the space. This allows faster convergence to optimal parameters compared to the conventional scan-based approach in fewer runs.

We note that the samples collected during GP optimization are insufficient to accurately extract the correlation matrix in the region surrounding the cost extrema; this is due to the low sample count required for convergence.

C. Constrained optimization

Our constrained optimization method is built upon the standard Lagrange multiplier (LM) technique. While this approach is analytically straightforward, its implementation in a data-sparse setting with experimental noise requires special consideration.

For the case of a single constraint $f(\mathbf{x}) = 0$ the LM

method first introduces a new cost function $C_{\text{LM}}(\mathbf{x}) = C(\mathbf{x}) + \lambda f(\mathbf{x})$, where the coefficient λ is the LM. As usual, local minima of C_{LM} occur at points of zero gradient

$$\nabla_{\mathbf{x}} C_{\text{LM}}(\mathbf{x}) = \nabla_{\mathbf{x}} C(\mathbf{x}) + \lambda \nabla_{\mathbf{x}} f(\mathbf{x}) = 0. \quad (2)$$

In conjunction with the constraint $f(\mathbf{x}) = 0$, this yields $n + 1$ coupled equations: sufficient to resolve the $n = \dim(\mathbf{x})$ components of \mathbf{x} along with the LM λ . The gradient of the constraint $\nabla_{\mathbf{x}} f(\mathbf{x})$ can be directly evaluated analytically since the constraint is known. In contrast, $\nabla_{\mathbf{x}} C(\mathbf{x})$ is an experimental quantity which can be estimated either by line scans or more efficiently via random sampling in the neighborhood of \mathbf{x} .

The strategy for updating the parameter vector $\mathbf{x}^{(n)}$ at iteration n to $\mathbf{x}^{(n+1)}$ proceeds as follows. First, we estimate the cost function and its gradient at $\mathbf{x}^{(n)}$ using a sampling strategy as discussed in Sec. IV A above, and obtain the gradient $\nabla_{\mathbf{x}} f(\mathbf{x}^{(n)})$ from a linear fit to the data. We then employ a constrained gradient descent to update $\mathbf{x}^{(n+1)} = \mathbf{x}^{(n)} + \beta \mathbf{P}_f \nabla_{\mathbf{x}} C(\mathbf{x}^{(n)})$ with convergence parameter β and \mathbf{P}_f projects onto the surface where $f(\mathbf{x}) = 0$. Separately, we solve the n linear equations in Eq. (2), each with a separate λ_i as the unknown quantity. These λ_i ’s will be equal only when $\mathbf{x}^{(n)}$ is an exceptional point of the constrained optimization problem. The optimization therefore terminates when $|\lambda_i - \lambda_j| < \epsilon$ for all i, j .

We demonstrate this procedure by optimizing the duration of each evaporation stage while constraining their sum: the total evaporation time T . Without the constraint, the optimal evaporation sequence would balance improved thermalization (favoring longer durations) and vacuum-limited lifetime (favoring shorter durations). Constraining the total duration therefore strategically exchanges time amongst stages in a way that optimizes BEC production.

For our specific linear constraint $f(t_1, \dots, t_n) = \sum_i t_i - T = 0$, Eq. (2) gives $\lambda_i = -\partial_{t_i} C(t_1, \dots, t_n)$. The gradient descent process can be thus be reframed as a re-weighting process in which the duration of stages with small λ_i are reduced, while the duration of stages with large λ_i are increased. This process is rapidly convergent, usually within three iterations; we tune α at each step to ensure $\sum_j |t_j^{(n)} - t_j^{(n+1)}| = 0.6$ s and terminate when $|\lambda_i - \lambda_j|$ is smaller than the largest uncertainties in all λ_i ’s. In practice, we perform a final stage of GP optimization (with durations) after completing the constrained optimization process, however, at best this yields a marginal improvement.

Figure 6 shows performance improvement of this process (red) compared to simply proportional scaling the stage durations (blue) for sequences with constrained evaporation durations from 7 s to 12 s. The bar-graphs in Fig. 6 show how this process fractionally redistributes time between the different stages. As the evaporation duration is reduced the fraction of time allocated to hybrid trap evaporation (blue) is reduced and redistributed to the rf evaporation stage (red).

We fully automated this process using our `labscript`-based experiment control system, with supporting code available online⁵⁴.

V. CONCLUSION

Here we described an apparatus that produces large sodium BECs in a hybrid trap, and describe efficiency gains achieved via parameter grouping, GP optimization, and LM-based constrained optimization. This integrated approach strikes a practical balance between performance of the optimization system while still benefiting from correlations between parameters. This enabled our BEC apparatus to outperform existing sodium BEC systems in terms of BEC production efficiency as a function of evaporation time (see Fig. 1).

Our automated time re-weighting protocol, based on constrained optimization, efficiently redistributes the evaporation sequence under fixed time constraints, significantly enhancing BEC quality by shifting resources from less effective to more impactful stages. In the results presented here, we minimized the sequence duration with fixed MOT parameters, arguing that the MOT and evaporation stages are largely decoupled. In reality these stages are correlated (albeit weakly); this correlation can be leveraged to even more effectively reduce the total sequence duration. For example, increasing the initial number of laser cooled atoms increases the collision rate in the magnetic trap, allowing for more rapid evaporation. So in such a situation, our LM technique may well sacrifice evaporation time for added MOT loading time.

ACKNOWLEDGMENTS

The authors thank K. T. Hoang and R. Shrestha for carefully reading the manuscript, and J. V. Porto, S. Subhankar for initial discussions. This work was partially supported by the National Institute of Standards and Technology, and the National Science Foundation through the Quantum Leap Challenge Institute for Robust Quantum Simulation (grant OMA-2120757).

¹K. B. Davis, M.-O. Mewes, M. R. Andrews, N. J. van Druten, D. S. Durfee, D. Kurn, and W. Ketterle, “Bose-Einstein condensation in a gas of sodium atoms,” *Phys. Rev. Lett.* **75**, 3969 (1995).

²M. H. Anderson, J. R. Ensher, M. R. Matthews, C. E. Wieman, and E. A. Cornell, “Observation of Bose-Einstein condensation in a dilute atomic vapor,” *Science* **269**, 198–201 (1995).

³I. Bloch, J. Dalibard, and W. Zwerger, “Many-body physics with ultracold gases,” *Rev. Mod. Phys.* **80**, 885 (2008).

⁴I. Bloch, J. Dalibard, and S. Nascimbene, “Quantum simulations with ultracold quantum gases,” *Nature Physics* **8**, 267–276 (2012).

⁵F. Schäfer, T. Fukuhara, S. Sugawa, Y. Takasu, and Y. Takahashi, “Tools for quantum simulation with ultracold atoms in optical lattices,” *Nature Reviews Physics* **2**, 411–425 (2020).

⁶H. Ritsch, P. Domokos, F. Brennecke, and T. Esslinger, “Cold atoms in cavity-generated dynamical optical potentials,” *Rev. Mod. Phys.* **85**, 553 (2013).

⁷M. A. Cazalilla, R. Citro, T. Giamarchi, E. Orignac, and M. Rigol, “One dimensional bosons: From condensed matter systems to ultracold gases,” *Rev. Mod. Phys.* **83**, 1405 (2011).

⁸T. Langen, R. Geiger, and J. Schmiedmayer, “Ultracold atoms out of equilibrium,” *Annu. Rev. Condens. Matter Phys.* **6**, 201–217 (2015).

⁹N. Navon, R. P. Smith, and Z. Hadzibabic, “Quantum gases in optical boxes,” *Nature Physics* **17**, 1334–1341 (2021).

¹⁰L. Amico, D. Anderson, M. Boshier, J.-P. Brantut, L.-C. Kwek, A. Minguzzi, and W. von Klitzing, “Colloquium: Atomtronic circuits: From many-body physics to quantum technologies,” *Rev. Mod. Phys.* **94**, 041001 (2022).

¹¹A. Tononi and L. Salasnich, “Low-dimensional quantum gases in curved geometries,” *Nature Reviews Physics* **5**, 398–406 (2023).

¹²O. Lahav, A. Itah, A. Blumkin, C. Gordon, S. Rinott, A. Zayats, and J. Steinhauer, “Realization of a sonic black hole analog in a Bose-Einstein condensate,” *Phys. Rev. Lett.* **105**, 240401 (2010).

¹³J. Steinhauer, “Observation of self-amplifying hawking radiation in an analogue black-hole laser,” *Nature Physics* **10**, 864–869 (2014).

¹⁴J. Steinhauer, “Observation of quantum hawking radiation and its entanglement in an analogue black hole,” *Nature Physics* **12**, 959–965 (2016).

¹⁵S. Eckel, A. Kumar, T. Jacobson, I. B. Spielman, and G. K. Campbell, “A rapidly expanding Bose-Einstein condensate: An expanding universe in the lab,” *Phys. Rev. X* **8**, 021021 (2018).

¹⁶J. R. Muñoz de Nova, K. Golubkov, V. I. Kolobov, and J. Steinhauer, “Observation of thermal hawking radiation and its temperature in an analogue black hole,” *Nature* **569**, 688–691 (2019).

¹⁷V. I. Kolobov, K. Golubkov, J. R. Muñoz de Nova, and J. Steinhauer, “Observation of stationary spontaneous hawking radiation and the time evolution of an analogue black hole,” *Nature Physics* **17**, 362–367 (2021).

¹⁸M. G. Galan, H. Sosa-Martinez, M. Anderson, and I. Spielman, “Accurate determination of hubble attenuation and amplification in expanding and contracting cold-atom universes,” *Phys. Rev. Lett.* **128**, 090401 (2022).

¹⁹C. Viermann, M. Sparn, N. Liebster, M. Hans, E. Kath, Á. Parra-López, M. Tolosa-Simeón, N. Sánchez-Kuntz, T. Haas, H. Strobel, *et al.*, “Quantum field simulator for dynamics in curved spacetime,” *Nature* **611**, 260–264 (2022).

²⁰A. Zenesini, A. Berti, R. Cominotti, C. Rogora, I. G. Moss, T. P. Billam, I. Carusotto, G. Lamporesi, A. Recati, and G. Ferrari, “False vacuum decay via bubble formation in ferromagnetic superfluids,” *Nature Physics*, 1–6 (2024).

²¹G. Santarelli, C. Audoin, A. Makdissi, P. Laurent, G. Dick, and A. Clairon, “Frequency stability degradation of an oscillator slaved to a periodically interrogated atomic resonator,” *IEEE Transactions on Ultrasonics, Ferroelectrics, and Frequency Control* **45**, 887–894 (1998).

²²K. Van der Stam, E. Van Ooijen, R. Meppelink, J. Vogels, and P. Van der Straten, “Large atom number Bose-Einstein condensate of sodium,” *Rev. Sci. Instrum.* **78** (2007), 10.1063/1.2424439.

²³E. Mimoun, L. D. Sarlo, D. Jacob, J. Dalibard, and F. Gerbier, “Fast production of ultracold sodium gases using light-induced desorption and optical trapping,” *Phys. Rev. A* **81**, 023631 (2010).

²⁴J. Jiang, L. Zhao, M. Webb, N. Jiang, H. Yang, and Y. Liu, “Simple and efficient all-optical production of spinor condensates,” *Phys. Rev. A* **88**, 033620 (2013).

²⁵W. Liu, N. Zheng, X. Wang, J. Xu, Y. Li, V. B. Sovkov, P. Li, Y. Fu, J. Wu, J. Ma, L. Xiao, and S. Jia, “Fast, simple, all-optical production of sodium spinor condensates,” *Journal of Physics B: Atomic, Molecular and Optical Physics* **54**, 155501 (2021).

²⁶J.-y. Choi, M.-S. Heo, and Y.-i. Shin, “Experimental apparatus for producing large ²³Na Bose-Einstein condensates,” *Journal of*

the Korean Physical Society **59** (2011), 10.3938/jkps.59.211.

²⁷G. Colzi, E. Fava, M. Barbiero, C. Mordini, G. Lamporesi, and G. Ferrari, “Production of large Bose-Einstein condensates in a magnetic-shield-compatible hybrid trap,” *Phys. Rev. A* **97**, 053625 (2018).

²⁸A. Farolfi, *Spin dynamics in two-component Bose-Einstein condensates*, Ph.D. thesis, Università degli studi di Trento (2021).

²⁹E. W. Streed, A. P. Chikkatur, T. L. Gustavson, M. Boyd, Y. Torii, D. Schneble, G. K. Campbell, D. E. Pritchard, and W. Ketterle, “Large atom number Bose-Einstein condensate machines,” *Rev. Sci. Instrum.* **77** (2006), 10.1063/1.2163977.

³⁰Z. Shi, Z. Li, P. Wang, K. S. Nawaz, L. Chen, Z. Meng, L. Huang, and J. Zhang, “Production of ²³Na Bose-Einstein condensates in the $F = 2$ state using D2 gray molasses,” *J. Opt. Soc. Am. B* **38**, 1229–1234 (2021).

³¹W. Hänsel, P. Hommelhoff, T. Hänsch, and J. Reichel, “Bose-Einstein condensation on a microelectronic chip,” *Nature* **413**, 498–501 (2001).

³²D. M. Farkas, E. A. Salim, and J. Ramirez-Serrano, “Production of rubidium Bose-Einstein condensates at a 1 Hz rate,” *arXiv preprint arXiv:1403.4641* (2014), 10.48550/arXiv.1403.4641.

³³Y.-J. Lin, A. R. Perry, R. L. Compton, I. B. Spielman, and J. V. Porto, “Rapid production of ⁸⁷Rb Bose-Einstein condensates in a combined magnetic and optical potential,” *Phys. Rev. A* **79** (2009), 10.1103/physreva.79.063631.

³⁴G. Colzi, G. Durastante, E. Fava, S. Serafini, G. Lamporesi, and G. Ferrari, “Sub-Doppler cooling of sodium atoms in gray molasses,” *Phys. Rev. A* **93**, 023421 (2016).

³⁵M.-S. Heo, J.-y. Choi, and Y.-i. Shin, “Fast production of large ²³Na Bose-Einstein condensates in an optically plugged magnetic quadrupole trap,” *Phys. Rev. A* **83**, 013622 (2011).

³⁶P. B. Wigley, P. J. Everitt, A. van den Hengel, J. W. Bastian, M. A. Sooriyabandara, G. D. McDonald, K. S. Hardman, C. D. Quinlivan, P. Manju, C. C. Kuhn, *et al.*, “Fast machine-learning online optimization of ultra-cold-atom experiments,” *Scientific Reports* **6**, 25890 (2016).

³⁷Z. Vendeiro, J. Ramette, A. Rudelis, M. Chong, J. Sinclair, L. Stewart, A. Urvoy, and V. Vuletić, “Machine-learning-accelerated Bose-Einstein condensation,” *Phys. Rev. Res.* **4**, 043216 (2022).

³⁸E. T. Davletov, V. V. Tsyganok, V. A. Khlebnikov, D. A. Pershin, D. V. Shaykin, and A. V. Akimov, “Machine learning for achieving Bose-Einstein condensation of thulium atoms,” *Phys. Rev. A* **102**, 011302 (2020).

³⁹R. Roussel, A. L. Edelen, T. Boltz, D. Kennedy, Z. Zhang, F. Ji, X. Huang, D. Ratner, A. S. Garcia, C. Xu, J. Kaiser, A. F. Pousa, A. Eichler, J. O. Lübsen, N. M. Isenberg, Y. Gao, N. Kuklev, J. Martinez, B. Mustapha, V. Kain, C. Mayes, W. Lin, S. M. Liuzzo, J. St. John, M. J. Streeter, R. Lehe, and W. Neiswanger, “Bayesian optimization algorithms for accelerator physics,” *Phys. Rev. Accelerators and Beams* **27** (2024), 10.1103/physrevaccelbeams.27.084801.

⁴⁰S. Banik, *Analogue Cosmology Experiments with Sodium Bose-Einstein Condensates*, Ph.D. thesis, University of Maryland (2021).

⁴¹M. Gutierrez Galan, *Bose Einstein Condensates for Analogue Cosmology Experiments*, Ph.D. thesis, University of Maryland (2021).

⁴²G. Lamporesi, S. Donadello, S. Serafini, and G. Ferrari, “Compact high-flux source of cold sodium atoms,” *Rev. Sci. Instrum.* **84** (2013), 10.1063/1.4808375.

⁴³Certain equipment, instruments, software, or materials are identified in this paper in order to specify the experimental procedure adequately. Such identification is not intended to imply recommendation or endorsement of any product or service by NIST, nor is it intended to imply that the materials or equipment identified are necessarily the best available for the purpose.

⁴⁴T. G. Tiecke, S. D. Gensemer, A. Ludewig, and J. T. M. Walraven, “High-flux two-dimensional magneto-optical-trap source for cold lithium atoms,” *Phys. Rev. A* **80** (2009), 10.1103/physreva.80.013409.

⁴⁵A. Gozzini, F. Mango, J. Xu, G. Alzetta, F. Maccarrone, and R. Bernheim, “Light-induced ejection of alkali atoms in polysiloxane coated cells,” *Il Nuovo Cimento D* **15**, 709–722 (1993).

⁴⁶G. Telles, T. Ishikawa, M. Gibbs, and C. Raman, “Light-induced atomic desorption for loading a sodium magneto-optical trap,” *Phys. Rev. A* **81**, 032710 (2010).

⁴⁷W. Ketterle, K. B. Davis, M. A. Joffe, A. Martin, and D. E. Pritchard, “High densities of cold atoms in a dark spontaneous-force optical trap,” *Phys. Rev. Lett.* **70**, 2253–2256 (1993).

⁴⁸P. D. Lett, R. N. Watts, C. I. Westbrook, W. D. Phillips, P. L. Gould, and H. J. Metcalf, “Observation of atoms laser cooled below the Doppler limit,” *Phys. Rev. Lett.* **61**, 169 (1988).

⁴⁹D. M. Stamper-Kurn, H.-J. Miesner, A. P. Chikkatur, S. Inouye, J. Stenger, and W. Ketterle, “Reversible formation of a Bose-Einstein condensate,” *Phys. Rev. Lett.* **81**, 2194–2197 (1998).

⁵⁰C. J. Pethick and H. Smith, *Bose-Einstein Condensation in Dilute Gases* (Cambridge University Press, 2001).

⁵¹P. T. Sivaprasad, F. Mai, T. Vogels, M. Jaggi, and F. Fleuret, “Optimizer benchmarking needs to account for hyperparameter tuning,” in *Proceedings of the 37th International Conference on Machine Learning*, Proceedings of Machine Learning Research, Vol. 119, edited by H. D. III and A. Singh (PMLR, 2020) pp. 9036–9045.

⁵²A. J. Barker, H. Style, K. Luksch, S. Sunami, D. Garrick, F. Hill, C. J. Foot, and E. Bentine, “Applying machine learning optimization methods to the production of a quantum gas,” *Machine Learning: Science and Technology* **1**, 015007 (2020).

⁵³P. T. Starkey, C. J. Billington, S. P. Johnstone, M. Jasperse, K. Helmerson, L. D. Turner, and R. P. Anderson, “A scripted control system for autonomous hardware-timed experiments,” *Rev. Sci. Instrum.* **84**, 85111 (2013).

⁵⁴Code is available at <https://github.com/JQIamo/labscript-time-reweight-optimization>.